A SHAPE OPTIMIZATION APPROACH FOR INFERRING SOURCES OF VOLCANO GROUND DEFORMATION

T. PERROT[1,2], F. SIGMUNDSSON[1] AND C. DAPOGNY[3]

[1] *Nordic Volcanological Center, Institute of Earth Sciences, University of Iceland, Reykjavík, Iceland.*
[2] *Mechanical engineering department, Ecole Normale Supérieure Paris-Saclay, Gif-sur-Yvette, France.*
[3] *Sorbonne Université, Université Paris Cité, CNRS, Inria, Laboratoire Jacques-Louis Lions, LJLL, F-75005 Paris, France.*

Abstract. One of the main goals of volcano geodesy is to improve the understanding of how an increase in pressure related to magma accumulation causes ground deformation in order to evaluate volcanic unrest. The inversion methods used for this purpose rely on a parametrization of the shape of the crustal volume in which pressure changes due to magma inflow/outflow (the magma domain), to search for the optimal parameters that minimize the difference between model predicted and measured ground displacements. However, these methods assume a predefined shape of the magma domain, which limits their applicability. Here, we propose a new shape optimization framework that can invert these sources without such prior, formulating a reconstruction problem to infer the complete shape of the magma domain. First, we validate this approach using a synthetic test case and then apply it to observations of the Svartsengi volcanic system in Iceland.

plain language summary. Volcanic magma domains contain pressurized magma that can feed eruptions when it breaks through. Volcanologists use measurements of the displacement of the surface of the Earth caused by increased pressure in magma domains to determine their location, shape, and pressure, which is crucial for evaluating eruption likelihood. They use methods in which they assume a physical model based on the domain's shape and pressure parameters, and then determine the set of parameters for which their model best predicts the measured displacements. However, these methods have a drawback in that they rely on the prior identification of relevant parameters for the shape of the magma domain, which is assumed to be "simple" (e.g., a sphere defined by its radius and center). This article introduces a new method for reconstructing the complex shape of a magma domain without first assuming a simple shape. The method is based on shape optimization, a widely used engineering framework for improving the design of mechanical parts with respect to requirements such as rigidity, vibration, etc. We validate our method using synthetic ground motion data and then apply it to real data from the Svartsengi volcanic system in Iceland.

Contents

1. Introduction

The accumulation of magma in volcano roots prior to eruptions may take place in diverse structures such as isolated magma chambers, reservoirs, and lenses, forming complex magmatic systems. We here refer to these crustal volumes as magma domains, that may consist of magma mush, liquid magma and hot rock. Improving understanding of the shape of magma domains where pressure increases is a major task in volcano geodesy.

Using volcano geodesy, the shape of a magma domain is often inferred from the resolution of an inverse problem, based on measurements of the ground deformation, obtained by Global Navigation Satellite System (GNSS) point positioning or Interferometric analysis of Synthetic Aperture Radar satellite images (InSAR). The source of deformation to be identified is commonly modeled by a vector $\mathbf{m}$ of d free parameters, which can be its spatial position, given by the three-dimensional (3D) coordinates of its center, its volume, the pressure inside, or other shape parameters. See e.g. [27, 43] and [40]. An $\mathbf{m}$-dependent "forward model" is then introduced to predict the deformation of the ground surface caused by such a source. The formulation of the latter may be analytic, assuming that the cavity has a "simple" shape, such as a point, spherical or elliptical source [27, 26, 46] embedded in a homogeneous elastic half-space. See also [30] for the situation of a rectangular plane with opening, reproducing the formation of magmatic sheets – dikes and sills. More general and complex types of cavities and constitutive laws of the crust have to be addressed by rather expensive numerical models based e.g. on the Finite Element Method (FEM). In any case, the shape parameters $\mathbf{m}$ are found by minimizing an objective function $J(\mathbf{m})$ measuring the misfit between a collection of real measurements of the displacement of the ground and the prediction of the model. Various mathematical optimization strategies are available to achieve this goal: global optimization methods, based on analytic [13] or numerical models [24, 14], Bayesian inference [6, 43], or genetic algorithms [45]. The aforementioned methods require an a priori parametrization of the shape of the source, and their reconstruction capabilities are intrinsically limited to the relevance of the chosen parameters: for instance, a method based on the identification of the radius of a spherical cavity cannot retrieve more complex shapes.

We here propose an alternative approach, combining a Finite Element forward model with a "free-form" shape optimization algorithm. Contrary to the aforementioned practice of parametric inversion, shape optimization deals with problems where the optimization variable is the shape of an object as a whole, that is, a 3D domain without the need for a parametrization [1, 3, 5, 9, 35]. Such level of abstraction involves advanced mathematical concepts, notably that of shape derivatives, as well as intricate numerical methods: "shape gradient" algorithms and the Level Set Method for tracking the motion of shapes, among others. On the other hand, it allows for an unprecedented freedom in the shape of the reconstructed magma domain, independent of an a priori parametrization. Shape and topology optimization is a popular practice in engineering, where one typically wishes to improve the design of an object to optimally meet a physical criterion. It spans various applications such as structural mechanics, where one often aims to improve the stiffness of a solid structure [8], fluid mechanics, where it is applied to the design of pipes, heat exchangers or flying obstacles [19], and even in electromagnetism [25], at both academic and industrial levels.

Multiple numerical frameworks are available for shape and topology optimization, see e.g. the review by [39]. Here, we use a method developed by [2], combining a so-called shape gradient optimization with a Level Set representation of shapes and a remeshing algorithm. We first present the method, then apply it to a test case and we eventually demonstrate its performance using real observational data.

2. Method

This section describes the proposed shape optimization formulation for the reconstruction of a magma domain and provides some details about our numerical implementation.

2.1. **Physical Model**

The Earth is modeled as a homogeneous and isotropic elastic medium, enclosing the magma domain whose shape is to be reconstructed. The boundary of the latter is subjected to a pressure change caused by the inflow of new magma; the elastic crust deforms instantaneously as a result and a new equilibrium is established. In particular, this phenomenon induces a deformation of the surface that can be measured.

This situation is formalized as follows, see Fig. 1a for an illustration. The geographical region of interest is represented by a fixed 3D domain D bounded by its boundary ∂D. D is made of two complementary subdomains Ω_{m} and Ω_{c}. The inner domain Ω_{m} represents the magma domain. Its boundary $\Gamma = \partial\Omega_{\mathrm{m}}$ is subject to the force $\Delta P \mathbf{n}_{\mathrm{m}}$ induced by the variation of pressure ΔP caused by the inflow/outflow of magma; this force is aligned with the unit normal vector $\mathbf{n}_{\mathrm{m}}$ to Γ pointing outward from Ω_{m}. The complementary subdomain Ω_{c} represents a portion of the surrounding Earth's crust. The displacement of the bottom side Γ_b of ∂D is set to zero and the other boundaries of D are free of stress. For convenience, we denote $\Omega = \Omega_{\mathrm{m}}$, and $\mathbf{n} = \mathbf{n}_{\mathrm{m}} = -\mathbf{n}_{\mathrm{c}}$ is the unit normal vector to Γ, pointing outward Ω_{m}. See Table S1 in Supporting Information for a list of symbols and nomenclature.

The displacement of the crust in these circumstances is denoted by $\mathbf{u}_\Omega$, where the subscript $_\Omega$ hints at its dependence on the shape Ω of the magma domain. It is the solution to the system of linearized elasticity:

$$\begin{cases} -\mathrm{div}(\mathbb{A}\boldsymbol{\mathcal{E}}(\mathbf{u}_\Omega)) = \mathbf{0} & \text{in } \Omega_{\mathrm{c}}, \\ \mathbf{u}_\Omega = \mathbf{0} & \text{on } \Gamma_{\mathrm{b}}, \\ \mathbb{A}\boldsymbol{\mathcal{E}}(\mathbf{u}_\Omega)\mathbf{n}_{\mathrm{c}} = -\Delta P\, \mathbf{n}_{\mathrm{c}} & \text{on } \Gamma, \\ \mathbb{A}\boldsymbol{\mathcal{E}}(\mathbf{u}_\Omega)\mathbf{n} = \mathbf{0} & \text{on } \partial D \setminus \overline{\Gamma_{\mathrm{b}}}, \end{cases} \tag{2.1}$$

where $\boldsymbol{\mathcal{E}}(\mathbf{u}) = \frac{1}{2}(\nabla\mathbf{u} + \nabla\mathbf{u}^T)$ is the strain tensor associated with a displacement field $\mathbf{u}$ and $\mathbb{A}$ is the Hooke's tensor of the crust material. For an isotropic medium, we have:

$$\mathbb{A}\boldsymbol{\mathcal{E}} = 2\mu\boldsymbol{\mathcal{E}} + \lambda \mathrm{tr}(\boldsymbol{\mathcal{E}})\mathbf{I},$$

where $\mathbf{I}$ is the identity matrix and $\lambda = \frac{E\nu}{(1+\nu)(1-2\nu)}$ and $\mu = \frac{E}{2(1+\nu)}$, are the Lamé coefficients, depending on the Young's modulus E and Poisson's ratio ν.

2.2. **Shape Optimization for the Reconstruction of the Magma Body**

The shape Ω of the magma domain is unknown, and we aim to reconstruct it by minimizing the least-square discrepancy $J_{\mathrm{LS}}(\Omega)$ between the displacement field $\mathbf{u}_\Omega$ of the upper surface of the Earth Γ_{u}, as predicted by the mechanical model (2.1), and $\mathbf{u}_{\mathrm{obs}}$ observed by using e.g. InSAR and/or GNSS geodesy. Formally, we seek Ω as the solution to the following shape optimization problem:

$$\min_{\Omega \subset D} J_{\mathrm{LS}}(\Omega), \text{ where } J_{\mathrm{LS}}(\Omega) = \int_{\Gamma_{\mathrm{u}}} |\mathbf{u}_\Omega - \mathbf{u}_{\mathrm{obs}}|^2 \, \mathrm{d}s. \tag{2.2}$$

2.3. **Shape Derivatives**

The treatment of Problem (2.2) calls for a notion of derivative for a function $J(\Omega)$ of the domain Ω. In this work, we rely on the boundary variation method of Hadamard [1, 3, 23, 28, 42]. It hinges on perturbations $\Omega_{\boldsymbol{\theta}}$ of a reference configuration Ω of the magma domain by a "small" vector fields $\boldsymbol{\theta}$: each point $\mathbf{x}_\theta$ in $\Omega_{\boldsymbol{\theta}}$ is obtained as the perturbed version of its counterpart $\mathbf{x}$ in Ω, as (see Fig. 1b):

$$\mathbf{x}_\theta = \mathbf{x} + \boldsymbol{\theta}(\mathbf{x}). \tag{2.3}$$

The shape derivative $J'(\Omega)(\boldsymbol{\theta})$ of a function $J(\Omega)$ at Ω in a direction $\boldsymbol{\theta}$ is the derivative of the mapping $\boldsymbol{\theta} \mapsto J(\Omega_{\boldsymbol{\theta}})$, so that the following Taylor approximation holds true:

$$J(\Omega_{\boldsymbol{\theta}}) \approx J(\Omega) + J'(\Omega)(\boldsymbol{\theta}). \tag{2.4}$$

In practice, $J'(\Omega)(\boldsymbol{\theta})$ is used to identify a descent direction $\boldsymbol{\theta}_{\mathbf{d}}$, i.e. a vector field such that $J'(\Omega)(\boldsymbol{\theta}_{\mathbf{d}}) < 0$. This property guarantees that, for a "small" step $\tau > 0$, we have:

$$J(\Omega_{\tau\boldsymbol{\theta}_{\mathbf{d}}}) \approx J(\Omega) + \tau J'(\Omega)(\boldsymbol{\theta}_{\mathbf{d}}) < J(\Omega), \tag{2.5}$$

in other words, the perturbed shape $\Omega_{\tau\boldsymbol{\theta}_{\mathbf{d}}}$ performs "better" than Ω in terms of the function $J(\Omega)$.

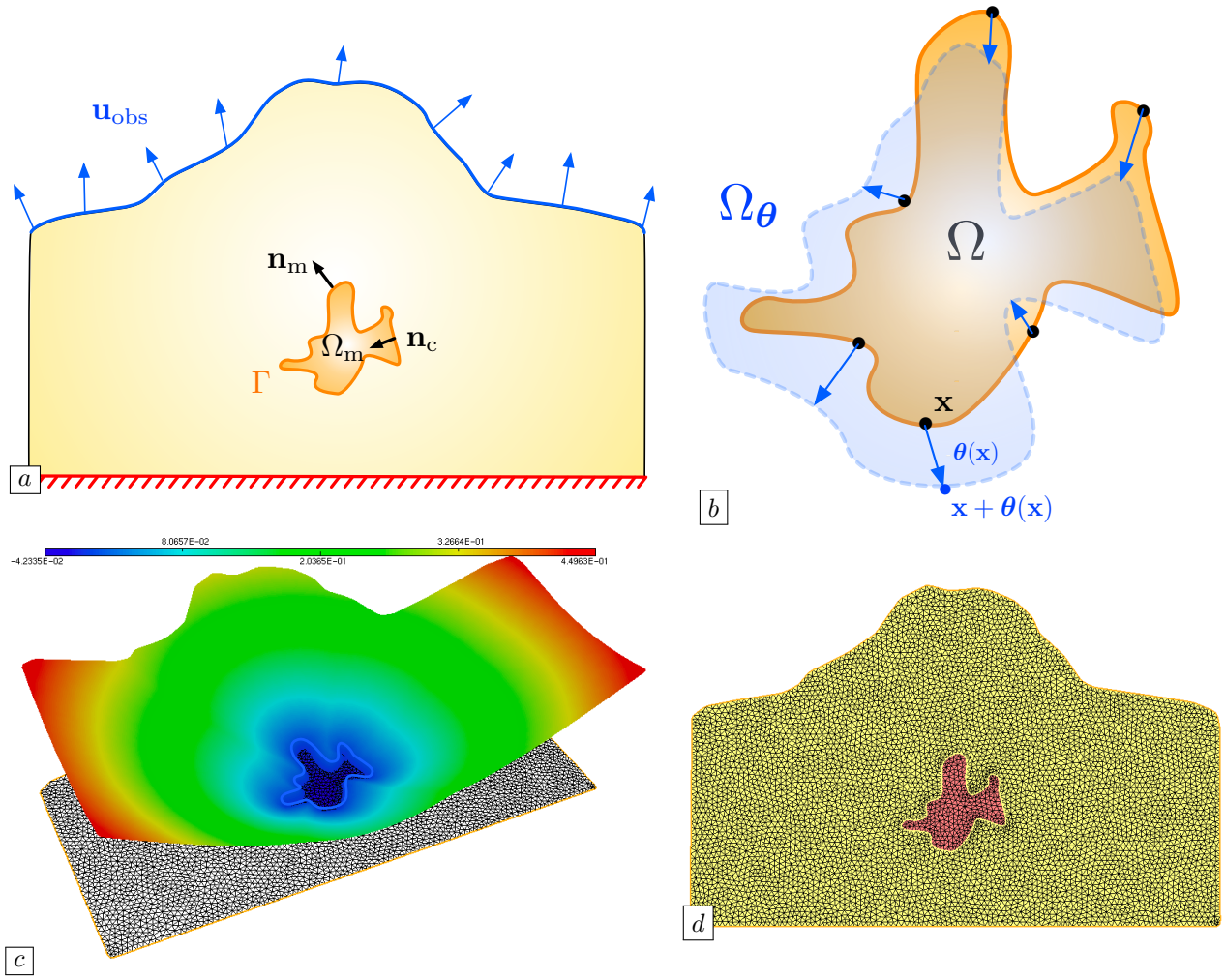

FIGURE 1. *(a) Sketch of the physical model, see the main text for the explanation. (b) Variation $\Omega_{\boldsymbol{\theta}}$ of Ω, according to the boundary variation method of Hadamard. (c) Graph of a level set function ϕ for the magma domain Ω. (d) Mesh of the geographical region D, comprising a mesh of Ω (in red) as a submesh.*

The identification of a descent direction for the functional $J_{\text{LS}}(\Omega)$ in (2.2) requires the explicit expression of its shape derivative. This calculation is a tedious, but classical issue in mathematics that can be realized thanks to the adjoint method, see e.g. [12, 37] and [4] in our particular mathematical context. It holds:

$$J'_{\text{LS}}(\Omega)(\boldsymbol{\theta}) = \int_{\Gamma} v_{\Omega}\,(\boldsymbol{\theta}\cdot\mathbf{n})\,\mathrm{d}s, \text{ where } v_{\Omega} = -\mathbb{A}\boldsymbol{\mathcal{E}}(\mathbf{u}_{\Omega}) : \boldsymbol{\mathcal{E}}(\mathbf{p}_{\Omega}) - \Delta P\,\mathrm{div}(\mathbf{p}_{\Omega}). \tag{2.6}$$

Here the so-called adjoint state $\mathbf{p}_{\Omega}$ is the vector field characterized by:

$$\begin{cases} -\mathrm{div}(\mathbb{A}\boldsymbol{\mathcal{E}}(\mathbf{p}_{\Omega})) = \mathbf{0} & \text{in } \Omega_{\text{c}}, \\ \mathbf{p}_{\Omega} = \mathbf{0} & \text{on } \Gamma_{\text{b}}, \\ \mathbb{A}\boldsymbol{\mathcal{E}}(\mathbf{p}_{\Omega})\mathbf{n}_{\text{c}} = \mathbf{0} & \text{on } \Gamma, \\ \mathbb{A}\boldsymbol{\mathcal{E}}(\mathbf{p}_{\Omega})\mathbf{n} = \mathbf{0} & \text{on } \partial D \setminus (\overline{\Gamma_{\text{u}}} \cup \overline{\Gamma_{\text{b}}}), \\ \mathbb{A}\boldsymbol{\mathcal{E}}(\mathbf{p}_{\Omega})\mathbf{n} = -2(\mathbf{u}_{\Omega} - \mathbf{u}_{\text{obs}}) & \text{on } \Gamma_{\text{u}}. \end{cases} \tag{2.7}$$

The adjoint state $\mathbf{p}_{\Omega}$ depends on the governing physics of the problem – linear elasticity – and on the quantity to be minimized $J_{\text{LS}}(\Omega)$. Intuitively, it behaves as a motion in the direction of a decrease of $J_{\text{LS}}(\Omega)$, but it

is above all a mathematical contrivance to endow the shape derivative $J'_{\mathrm{LS}}(\Omega)$ with a convenient expression. See Supporting Information Text S1 for the derivation of Equation (2.7).

A descent direction for $J_{\mathrm{LS}}(\Omega)$ is found from Equation (2.6) by choosing $\boldsymbol{\theta}_{\mathbf{d}} = -v_\Omega\,\mathbf{n}$:

$$J'(\Omega)(\boldsymbol{\theta}_{\mathbf{d}}) = -\int_\Gamma v_\Omega^2\,\mathrm{d}s < 0. \tag{2.8}$$

The above concepts pave the way to a shape gradient algorithm: starting from an initial shape Ω^0 of the magma domain, the least-square discrepancy $J_{\mathrm{LS}}(\Omega)$ is minimized through a series of iterations $n = 0, \dots$ where each shape Ω^n is updated as

$$\Omega^{n+1} = \Omega^n_{\tau^n \boldsymbol{\theta}_{\mathbf{d}}{}^n} = \left\{\mathbf{x} + \tau^n \boldsymbol{\theta}_{\mathbf{d}}{}^n(\mathbf{x}),\ \ \mathbf{x} \in \Omega^n\right\}, \tag{2.9}$$

where $\tau^n > 0$ is a "small" step and $\boldsymbol{\theta}_{\mathbf{d}}{}^n$ is the descent direction in (2.8), see Fig. 2.

2.4. Description of the Numerical Implementation

2.4.1. *Level Set Representation of the Shape*

The numerical realization of our shape gradient strategy raises the need for an efficient approach to represent the shape and its updates via the operation (2.9). To achieve this, we rely on the Level Set Method, pioneered in [32]. See also [31] and [38] for extensive presentations and [4] for its introduction in the field of shape optimization.

At each stage of the process, the magma domain Ω is described as the negative region of a scalar field ϕ, referred to as a "level set" function, with the following properties:

$$\text{For every point } \mathbf{x} \text{ in } D, \quad \begin{cases} \phi(\mathbf{x}) < 0 & \text{if } \mathbf{x} \in \Omega_{\mathrm{m}} = \Omega, \\ \phi(\mathbf{x}) = 0 & \text{if } \mathbf{x} \in \Gamma, \\ \phi(\mathbf{x}) > 0 & \text{if } \mathbf{x} \in \Omega_{\mathrm{c}} = D \setminus \overline{\Omega}, \end{cases} \tag{2.10}$$

see Fig. 1c for a 2D illustration.

The evolution of Ω between two consecutive shapes Ω^n and Ω^{n+1}, described by the respective Level Set functions ϕ^n, ϕ^{n+1}, under the velocity field $\boldsymbol{\theta}_{\mathbf{d}}{}^n(\mathbf{x})$ over the (pseudo-time) period $t \in (0, \tau^n)$ is captured by the following advection equation:

$$\phi^{n+1}(\mathbf{x}) = \psi(\tau^n, \mathbf{x}), \text{ where } \begin{cases} \dfrac{\partial \psi}{\partial t}(t,\mathbf{x}) + \boldsymbol{\theta}_{\mathbf{d}}{}^n(\mathbf{x}) \cdot \nabla \psi(t,\mathbf{x}) = 0 & \text{for } t \in (0,\tau^n),\ \mathbf{x} \in D, \\ \psi(t=0,\mathbf{x}) = \phi^n(\mathbf{x}) & \text{for } \mathbf{x} \in D. \end{cases} \tag{2.11}$$

Intuitively, this equation from fluid mechanics captures the transport of a quantity (such as a chemical) by a fluid.

2.4.2. *Coupling with a Remeshing Algorithm*

Our practical implementation leverages a recent variant of the Level Set method, introduced by [2], an open-source implementation of which is proposed in [16]. This method includes an additional ingredient: at each iteration $n \geq 0$ of the optimization process, a remeshing operation is conducted to create a meshed representation of the configuration, i.e. the magma and crust domains Ω^n_{m} and Ω^n_{c} are discretized as complementary submeshes of the total mesh $\mathcal{T}^n$ of D, see Fig. 1d. Note that this operation can be conducted so that the mesh $\mathcal{T}^n$ features a fine resolution where needed (notably, in the neighborhood of the shape Ω^n) and a coarse size elsewhere. This practice makes it possible to efficiently solve the numerical resolution of the state and adjoint equations (2.1) and (2.7) with a standard Finite Element software.

2.4.3. *Overview of the Algorithm*

Our numerical workflow is sketched in Fig. 2. Briefly, at each iteration n, the computational domain D is discretized by a mesh $\mathcal{T}^n$ which encloses a discretization of the actual shape Ω^n of the magma domain as a submesh. The initial mesh $\mathcal{T}^0$ is here created with the open-source software `Gmsh` [21], and the remeshing library `mmg` [7, 15] is used to remesh at the subsequent iterations. The elasticity and adjoint systems (2.1) and (2.7) for $\mathbf{u}_{\Omega^n}$ and $\mathbf{p}_{\Omega^n}$ are solved on this exact mesh by the open-source Finite Element library `FreeFem` [22]. A descent direction $\boldsymbol{\theta}_{\mathbf{d}}{}^n$ is then obtained via the formula (2.8). The update (2.9) of the shape is carried out according to the Level Set Method: a level set function ϕ^n for Ω^n is generated by the library `mshdist`

[17] and the advection equation (2.11) is solved for ϕ^{n+1} by using the open-source library `Advect` [10]. More details are provided in Supporting Text S2 about practical aspects of this numerical implementation. The associated code `magmaOpt` and a short documentation are available online [34].

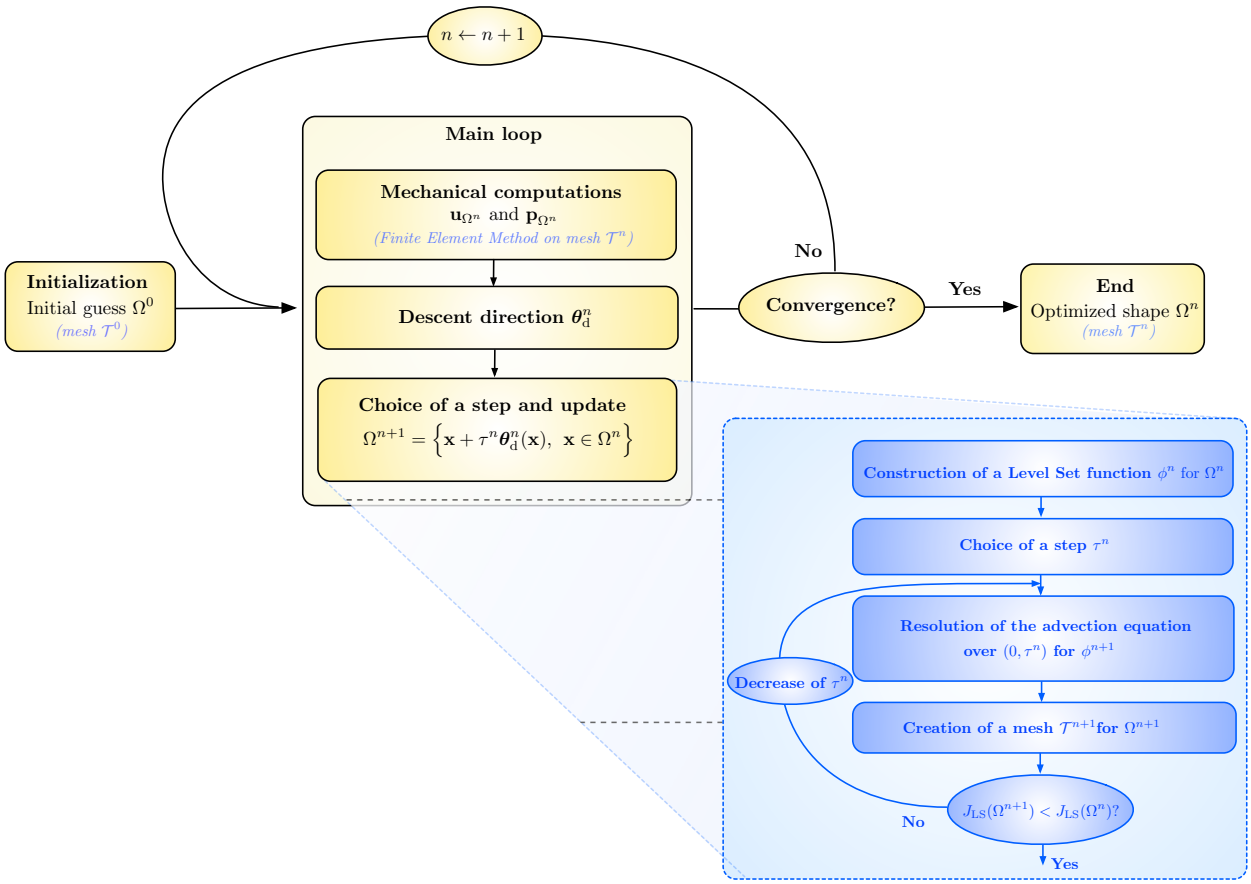

FIGURE 2. Overview of the shape optimization algorithm; the parts in blue provide further information about some operations.

3. RESULTS

3.1. Validation Using Synthetic Data

In a first validation example, an artificial surface displacement of the field is generated from a known spherical source Ω^* with radius 1 km, centered at $(2, 2, -2)$ km. The initial guess Ω^0 is an ellipsoid centered at $(-3, 0, -3)$km, with semi-axes r_x=1 km, r_y=r_z=2 km. The mechanical parameters are E=10 GPa, ν=0.25 and ΔP=2 MPa. The results of the computations are displayed in Fig. 3, and Supporting Movie S1 contains more details about the iterative process.

The iteratively modified shape Ω^n converges to the objective Ω^* after 1044 iterations, with an error of 1.1 m^4, corresponding to an average discrepancy $\sqrt{J_{\mathrm{LS}}(\Omega)/A(\Gamma_{\mathrm{u}})}$ ($A(\Gamma_{\mathrm{u}})$ being the area of the boundary Γ_{u}) between the predicted and objective displacement fields at the surface of the Earth of approximately 0.1 mm, to be compared with a maximum displacement of the ground surface of 78 mm (see Supporting Figure S1). Note that the solution process features quite unexpected intermediate shapes: at iteration 240, the shape splits into two parts, which merge at iteration 550. The step size τ^n, featured in (2.9) and (2.11) is large when the descent direction $\boldsymbol{\theta_{\mathrm{d}}}^n$ allows for a firm decrease of $J_{\mathrm{LS}}(\Omega)$ (which is the case at the beginning of the procedure), while on error plateaus, where only small modifications of the shape are possible (as after iteration $\sim$ 1000), the step size stagnates around its minimum value, fixed at 0.01.

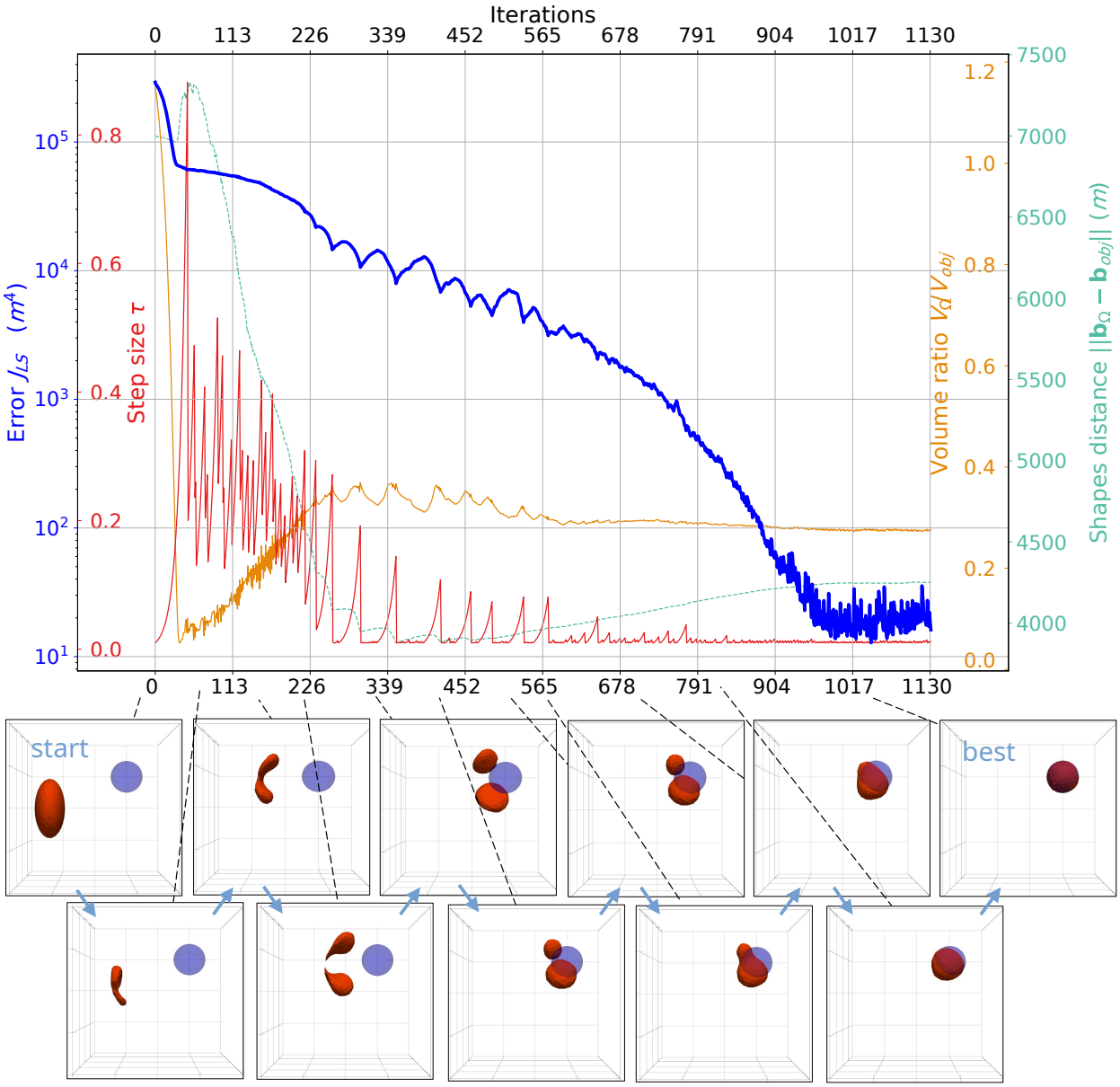

FIGURE 3. Convergence history of the synthetic reconstruction test case of Section 3.1. The value of the objective $J_{\mathrm{LS}}(\Omega^n)$ is displayed in logarithmic scale (blue); the step size τ^n is shown with red curve, the distance between the centroids of Ω^n and Ω^* is the orange curve, and the green dashed line represents the ratio between the volumes of Ω^n and Ω^*. The lower panels display top views of a few intermediate shapes Ω^n of the magma domain (in red), while the target shape Ω^* is the blue sphere.

Like any gradient-based optimization strategy, the present method is likely to fall into a local minimum of the objective function $J_{\mathrm{LS}}(\Omega)$. To try and mitigate this effect, insofar as possible, we do not require a strict decrease of the value of the objective function for setting the step τ^n, which explains for the slight increases in the error that occasionally occur. Additional discussions about the behavior of the optimization and tuning strategies are included in Section 4 and in Supporting Information Text S3. See also Supporting Figure S2 for the outcome of a different test case featuring a shape Ω^* made of two disconnected bodies.

With respect to the computational effort of the procedure, the Finite Element resolutions of the state and adjoint systems (2.1) and (2.7) are the most computationally intensive steps. The remeshing and advection operations are less demanding. Depending on the mesh size, one iteration can take a few seconds to several minutes; on this example, the CPU time stays lower than 10 seconds per iteration on a consumer grade laptop, for meshes containing about $10^5 - 10^6$ elements.

3.2. **Test Case: Magma Recharge at Svartsengi, 2022**

This second example illustrates the use of our reconstruction methodology with real data, spanning the ground inflation observed at Svartsengi (Iceland) from 21 April to 14 June, 2022. This event, analyzed by [40], was one of the five inflation episodes that preceded the initial diking event at the Sundhnúkur crater row on 10-12 November 2023, resulting in the partial destruction of the town of Grindavík.

The observational data are 6 ascending and descending unwrapped InSAR line-of-sight (LOS) displacement maps of the area, obtained from the COSMO-SkyMed, TerraSAR-X and Sentinel-1 satellites and made available by [33] and [40]. These data are downsampled and interpolated on the computational domain D – a cube with 20 km sides – meshed with an nominal edge size of 500 m. To accommodate these InSAR data, we use a slightly modified version $J_{\text{LS}}^{\text{los}}(\Omega)$ of the objective function in (2.2), see Supporting Text S4 for details. For the physical parameters, the elastic moduli in the crust are assumed to be homogeneous, with values $E = 25$ GPa and $\nu = 0.26$ [40]. Although uncertain, a pressure change of $\Delta P = 3$ MPa is here assumed on the magma domain boundary Γ, in line with the argumentation of [41] who put bounds on the total pre-diking pressure increase prior to the 10-12 November event.

The initial guess Ω^0 about the magma domain shape is a sphere of 2 km radius located at the local origin (see Fig. 4) at 5 km depth. The application of our methodology leads to the results shown in Fig. 4 and Supporting Movie S2. After 200 iterations, during which the error decreases sharply, only minor modifications are observed, corresponding to a small step size τ^n. The optimization process was stopped few hundred iterations after the best shape is found (iteration 772) without improvements. The associated value of the objective function equals 1.36×10^4 m^4, corresponding to an average discrepancy in the LOS displacement field of 6 mm on the surface. The total volume of the domain equals 34 km^3, and the corresponding volume change is $\Delta V = \int_\Gamma \mathbf{u}_\Omega ds = 12 \times 10^6$ m^3 at the assumed pressure change ΔP. In broad terms, the optimized magma domain is a thin East-West elongated, tilted body, 9.3 km long in the East-West direction, 3.8 km long in the North-South direction, with thickness ranging from 1 to 1.7 km, dipping approximately 32° towards South, with a barycenter located at $(0.7, 0.8, -7.5)$ km. This shape is made of 2 lobes, the eastern one being roughly spherical, while the western one is more elongated.

This complex optimized shape can be compared with the inversion results based on the same data presented in [40] and [33]. In these studies, a rectangular sill is reconstructed which is 6.3 km long and 0.6 km wide, with 92 cm opening, at a depth of 4.3 km, dipping 7.3° with a strike of $N56°E$. A volume change about 3 times smaller than in our study was found. Moreover, our magma domain is located deeper; it has a more elongated shape, with a higher dip. Following [27] and [26], it is known that the maximum uplift $u_z^{\max}$ generated by a spherical cavity scales as $u_z^{\max} \propto C = \Delta V / z^2$, where z is the depth of the center of the sphere. Reasoning at first order, i.e. approximating our magma domain shape by a McTigue-like solution, we obtain a ratio of $C_\Omega = 0.21$, while for the previous aforementioned studies, this quantity equals $C_{\text{sill}} = 0.18$. These values are comparable, suggesting that both models predict a ground surface displacement with similar amplitude, ours featuring a magma domain at a greater depth, with a greater volume change.

The assumed pressure ΔP has a significant influence on the optimal shape, as illustrated in Supporting Figures S3 and S4. These depict the results of the same inversion procedure, based on the same data, but with the different values, $\Delta P = 1$ MPa and 6 MPa. For the 6 MPa case, the reconstructed magma domain features approximately the same barycenter depth and volume change as in the 3 MPa case, whereas the overall magma domain volume is about twice as small (at equal depth, a higher pressure requires a lesser area of the magma domain boundary to produce similar surface deformation). The 1 MPa optimized shape is much more voluminous, and its proximity with the boundaries of the geographical region D may influence the reconstructed morphology. Nevertheless, the same trend is observed: a volume change of the same order (20×10^6 m^3) as the other test cases for a much larger volume. The resulting shapes are similar to those shown in Fig. 4 (East-West elongation, South dipping), but they have unequally complex outlooks. The

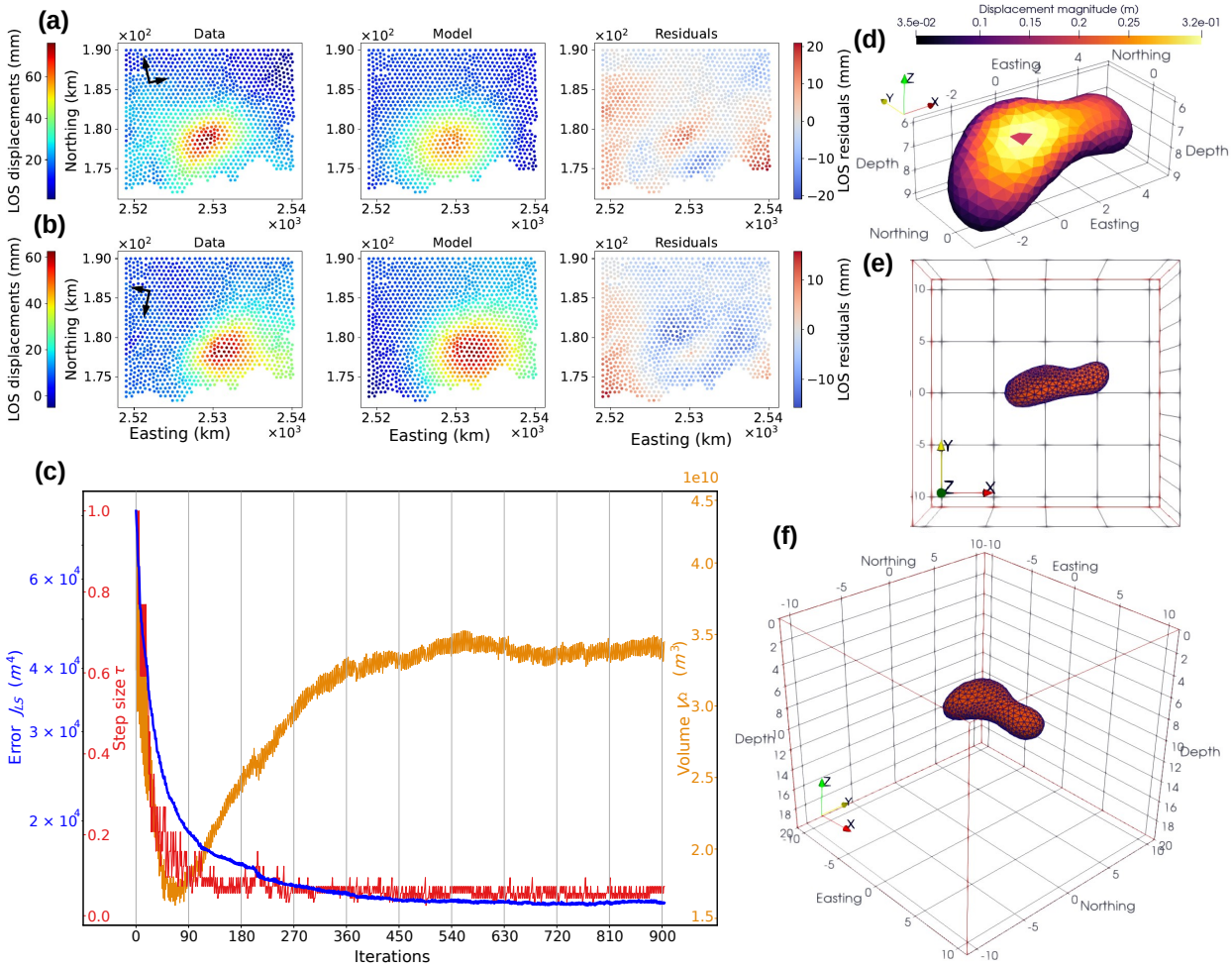

FIGURE 4. *Inversion of the shape of a magma domain based on the data from the Svarstengi 2022 inflation event. (a, b) Input LOS data, model LOS displacements for the optimized shape and residuals of the LOS displacements for the Sentinel-1 T16 (ascending, a) and T155 (descending, b) tracks. The black arrows indicate the satellite heading and look directions. Coordinates are in ISN16 Cartesian projection [44], centered at a local origin* ($25.3 \times 10^5 E$, 1.79×10^5 *N). See Supporting Figure S3 for the plots associated to the other tracks used in the inversion. (c) Convergence history, using identical symbols to those in in Fig. 3. (d, e, f) 3D views of the optimized shape (+X direction is East, +Y is North and −Z is Depth). (d) Magnitude of the displacement on the magma domain boundary. Top view (e) of the magma domain and 3D view (f), with the full computational domain outlined in red.*

higher the pressure change ΔP, the simpler the shape: because less volume is needed to produce similar displacements, less freedom is left to the optimization algorithm to explore for complex shapes.

4. DISCUSSION

This work illustrates a new class of methods for magma domain inversion which can reconstruct arbitrarily complex shapes without the need for an a priori parametrization. The promising, albeit preliminary results suggest several directions for further improvement.

First, in the present study, the pressure difference ΔP at the boundary of the magma domain is specified, although the results of multiple inversions associated to different pressure values can be compared. See

Supporting Information Figures S4-S5 about the influence of this parameter on the final shape. In more general situations, ΔP is unknown and should be reconstructed from the observational data, along with the shape Ω of the magma domain. A relatively simple adaptation of our reconstruction problem (2.2) and of the solution methodology exposed thereafter would allow to achieve this goal.

Another drawback of the proposed method, actually plaguing all gradient-based inversion strategies, lies in its trend to fall into one of the (many) local minima of the problem (2.2). The optimization path, and the resulting shape of the magma domain, is influenced by the choice of the numerical parameters, such as the mesh size, the optimization parameters, etc, see Supporting Text S3. Crucially, it also depends strongly on the initial guess Ω^0. Hence, the method presented here could advantageously be combined with classical analytical inversion methods, producing "simple", relevant initial regular shapes, to be further refined.

As for any inversion method, the quality of the reconstruction would benefit from the input of additional measurements, and more generally from the incorporation of different prior information about the shape, for instance under the form of constraints in the formulation (2.2), guided e.g. by estimates of the volume of the source, or about its depth, known from seismic or geochemical observations. See e.g. [18] for a constrained optimization algorithm to handle such treatment. On a different note, the "simple" linear elasticity model used in this work could be refined by taking into account the presence of external loads (such as tectonic stress), complex topographic geometries and a more elaborated and realistic mechanical behavior of the crust (such as depth varying values of elastic parameters or viscoelastic rheology).

From the software viewpoint, an obvious lead for improvement consists in increasing the resolution of the problem, e.g. by using a larger computational domain D (to reduce edge effects) and finer meshes, in combination with parallel FEM resolutions of the elasticity and adjoint systems, to keep a reasonable CPU cost.

5. Conclusion

We illustrate the application of shape optimization techniques to infer plausible scenarios about the geometry of a magma domain from measurements of the ground surface displacement field. The presented inversion result based on synthetic data is representative of the expected diversity and complexity faced by the algorithm in more realistic situations; it underlines the intrinsic non-uniqueness of solutions to the reconstruction problem, and shows that the method delivers consistent results when used with a suitable initial guess. The test on real data from the Svarstengi 2022 inflation inferred a complex shape capable of explaining well observations from six InSAR tracks. We here propose a new, free-form inversion method for volcano geodesy that can be further improved. The method has potential for general applications, and may contribute to better understanding of magmatic processes and forecasting of volcanic eruptions.

Open Research Section

The code developed and utilized in this paper, `magmaOpt`, is freely available at [34]. All the data used in the study of the 2022 Svartsengi inflation are publically available from the article [33].

Acknowledgements. The work of T.P. and F.S. is partially supported by the University of Iceland Research Fund. The work of C.D is partially supported by the projects ANR-24-CE40-2216 STOIQUES and ANR-22-CE46-0006 StableProxies. T.P. would like to thank Bogi Ingimundarson for his support during the early development of the method and for the insightful discussions about Icelandic volcanology. The authors thank Chiara Lanzi for providing additional details about the Svartsengi 2022 inflation data. The satellite data utilized in this study was originally provided through the GEO Geohazard Supersites and Natural Laboratory (GSNL) Icelandic Volcanoes Supersite project supported by the Committee on Earth Observing Satellites.

Appendix A. Supplementary material

This Supporting Information document describes a few technical details about our numerical algorithm for magma domain inversion, and it provides additional results. It contains text, figures, and supplementary movie files.

Table S1 provides a nomenclature summarizing all mathematical notations used in the main text.

Texts S1 to S4 aim to provide a better understanding of the method; they respectively deal with the precise technique used to extract a descent direction from the shape derivative of the objective function, additional ingredients of the shape optimization process, a description of possible descent behaviors, and a modified expression of the error functional for InSAR data.

Figures S1 to S4 complement the test cases presented in the main text with additional views of the results discussed in there, and illustrations of complementary results.

Finally, the movies illustrate how the method works by showing the successive shapes found by the algorithm during the descent procedure.

Table S1. Nomenclature and definitions

Symbol	Nature	Description
		Geometric entities
D	$\subset \mathbb{R}^3$	Total region of interest, including crust and magma domains
∂D	$\subset \mathbb{R}^3$	Boundary of D
$\Omega = \Omega_{\mathrm{m}}$	$\subset D$	Magma domain
Ω_{c}	$= D \setminus \overline{\Omega_{\mathrm{m}}}$	Crust surrounding the magma domain
Γ	$= \partial\Omega_{\mathrm{m}}$	3D surface of the magma body
Γ_{u}	$\subset \partial\Omega_{\mathrm{c}}$	Upper boundary of the crust (ground surface)
Γ_{b}	$\subset \partial\Omega_{\mathrm{c}}$	Bottom boundary of the crust
$\mathbf{n} = \mathbf{n}_{\mathrm{m}}$	$\Gamma \to \mathbb{R}^3$	Unit normal vector to Γ pointing outward Ω_{m}
$\mathbf{n}_{\mathrm{c}} = -\mathbf{n}_{\mathrm{m}}$	$\Gamma \to \mathbb{R}^3$	Unit normal vector to Γ pointing inward Ω_{m}
		System of linearized elasticity
$\mathbf{u}_\Omega$	$\Omega_{\mathrm{c}} \to \mathbb{R}^3$	Displacement field of the crust when the actual shape of the magma domain is Ω
$\boldsymbol{\mathcal{E}}(\mathbf{u})$	$= \frac{1}{2}(\nabla\mathbf{u} + \nabla\mathbf{u}^T)$	Linearized strain tensor induced by a displacement $\mathbf{u}$
$\mathbb{A}\boldsymbol{\mathcal{E}}$	$= 2\mu\boldsymbol{\mathcal{E}} + \lambda\mathrm{tr}(\boldsymbol{\mathcal{E}})\mathbf{I}$	Stress tensor within the isotropic material induced by a strain $\boldsymbol{\mathcal{E}}$
ΔP	$\in \mathbb{R}$	Pressure difference at the boundary of the magma domain
		Optimization procedure
$\mathbf{u}_{\mathrm{obs}}$	$\Gamma_{\mathrm{u}} \to \mathbb{R}^3$	Observed displacement of the ground surface
$J_{\mathrm{LS}}(\Omega)$	$\in \mathbb{R}$	Least-square discrepancy between the prediction $\mathbf{u}_\Omega$ and the observation $\mathbf{u}_{\mathrm{obs}}$ on Γ_u
$\boldsymbol{\theta}$	$\Gamma \to \mathbb{R}^3$	"Small" vector field used to modify a shape Ω
$\Omega_{\boldsymbol{\theta}}$		Perturbation of a shape Ω by a "small" vector field $\boldsymbol{\theta}$
$J'(\Omega)(\boldsymbol{\theta})$		Shape derivative of a function J at Ω, in a direction $\boldsymbol{\theta}$
$\boldsymbol{\theta}_{\mathbf{d}}$	$\Gamma \to \mathbb{R}^3$	Descent direction allowing for a decrease of $J(\Omega)$
$\mathbf{p}_\Omega$	$\Omega_{\mathrm{c}} \to \mathbb{R}^3$	Adjoint displacement field
ϕ	$D \to \mathbb{R}$	Level Set function used in the numerical method to track the changes in the boundary Γ
τ	$\in \mathbb{R}$	Step size of the gradient descent
$\mathcal{T}$		Mesh corresponding to the numerical discretization of D

Text S1. Calculation of the shape derivative of $J_{\mathrm{LS}}(\Omega)$ using Cea's method

For completeness, we provide a formal outline of the calculation of the shape derivative (2.8) of the function $J_{\mathrm{LS}}(\Omega)$ in (2.2). We essentially reproduce the argument from [4], based on Céa's method [12].

Let us first recall a classical result, which is often referred to as the Reynolds transport theorem in the physics literature, see e.g. [23].

Proposition A.1. *Let $f : \mathbb{R}^3 \to \mathbb{R}$ be a smooth function, and let $F(\Omega)$ be defined by:*

$$F(\Omega) := \int_\Omega f \,\mathrm{d}\boldsymbol{x}.$$

The shape derivative of the functional $F(\Omega)$ then reads:

$$F'(\Omega)(\boldsymbol{\theta}) = \int_\Gamma f(\boldsymbol{\theta}\cdot\boldsymbol{n})\,\mathrm{d}s,$$

where we recall that $\boldsymbol{n}$ is the unit normal vector to Γ, pointing outward Ω.

We now turn the proof of the formula (2.6), properly speaking. Let V be the space of vector-valued functions $\mathbf{u} : \mathbb{R}^3 \to \mathbb{R}$ vanishing on the region Γ_{b}, and let $\mathcal{L}(\Omega_{\mathrm{c}}, \cdot, \cdot) : V \times V \to \mathbb{R}$ be defined by:

$$\mathcal{L}(\Omega, \mathbf{u}, \mathbf{p}) = \int_{\Gamma_{\mathrm{u}}} |\mathbf{u} - \mathbf{u}_{\mathrm{obs}}|^2 \,\mathrm{d}s + \int_{\Omega_{\mathrm{c}}} \mathbb{A}\boldsymbol{\mathcal{E}}(\mathbf{u}) : \boldsymbol{\mathcal{E}}(\mathbf{p})\,\mathrm{d}\mathbf{x} + \Delta P \int_\Gamma \mathbf{p}\cdot\mathbf{n}_{\mathrm{c}}\,\mathrm{d}s. \tag{A.1}$$

Intuitively, $\mathcal{L}(\Omega, \mathbf{u}, \mathbf{p})$ is the Lagrangian associated to the minimization problem (2.2), in the equivalent formulation where the elasticity problem (2.1) for the displacement $\mathbf{u}_\Omega$ of the underground is seen as a constraint and $\mathbf{p}$ is the associated Lagrange multiplier, that is:

$$\min_{\Omega,\mathbf{u}} \int_{\Gamma_u} |\mathbf{u} - \mathbf{u}_{\mathrm{obs}}|^2 \,\mathrm{d}s \quad \text{s.t.} \quad \begin{cases} -\mathrm{div}(\mathbb{A}\boldsymbol{\mathcal{E}}(\mathbf{u})) = \mathbf{0} & \text{in } \Omega_{\mathrm{c}}, \\ \mathbf{u} = \mathbf{0} & \text{on } \Gamma_{\mathrm{b}}, \\ \mathbb{A}\boldsymbol{\mathcal{E}}(\mathbf{u})\mathbf{n}_{\mathrm{c}} = -\Delta P\,\mathbf{n}_{\mathrm{c}} & \text{on } \Gamma, \\ \mathbb{A}\boldsymbol{\mathcal{E}}(\mathbf{u})\mathbf{n} = \mathbf{0} & \text{on } \partial D \setminus \overline{\Gamma_{\mathrm{b}}}, \end{cases} \tag{A.2}$$

By construction, it holds:

$$\forall \mathbf{p} \in V, \quad J_{\mathrm{LS}}(\Omega) = \mathcal{L}(\Omega, \mathbf{u}_\Omega, \mathbf{p}). \tag{A.3}$$

Introducing a smooth function $\chi : \mathbb{R}^3 \to \mathbb{R}$, which equals 1 on Ω and 0 on ∂D, and applying the Green's formula, we may rewrite the last term in (A.1) as an integral over the domain Ω_{c}:

$$\mathcal{L}(\Omega, \mathbf{u}, \mathbf{p}) = \int_{\Gamma_{\mathrm{u}}} |\mathbf{u} - \mathbf{u}_{\mathrm{obs}}|^2 \,\mathrm{d}s + \int_{\Omega_{\mathrm{c}}} \mathbb{A}\boldsymbol{\mathcal{E}}(\mathbf{u}) : e(\mathbf{p})\,\mathrm{d}\mathbf{x} + \Delta P \int_{\Omega_{\mathrm{c}}} \mathrm{div}(\chi\mathbf{p})\,\mathrm{d}\mathbf{x}. \tag{A.4}$$

For a given shape Ω, $\mathbf{u}$ attains the minimum in (A.2) if there exists $\mathbf{p} \in V$ such that $(\mathbf{u}, \mathbf{p}) \in V \times V$ is a saddle point of the function $\mathcal{L}(\Omega, \cdot, \cdot)$. We then search for these saddle points. To achieve this, we equate the partial derivatives of $\mathcal{L}(\Omega, \cdot, \cdot)$ to 0. This yields:

$$\forall \widehat{\mathbf{p}} \in V, \quad \frac{\partial \mathcal{L}}{\partial \mathbf{p}}(\Omega, \mathbf{u}, \mathbf{p})(\widehat{\mathbf{p}}) = \int_{\Omega_{\mathrm{c}}} \mathbb{A}\boldsymbol{\mathcal{E}}(\mathbf{u}) : \boldsymbol{\mathcal{E}}(\widehat{\mathbf{p}})\,\mathrm{d}\mathbf{x} + \Delta P \int_\Gamma \widehat{\mathbf{p}}\cdot\mathbf{n}_{\mathrm{c}}\,\mathrm{d}s = 0, \tag{A.5}$$

and

$$\forall \widehat{\mathbf{u}} \in V, \quad \frac{\partial \mathcal{L}}{\partial \mathbf{u}}(\Omega, \mathbf{u}, \mathbf{p})(\widehat{\mathbf{u}}) = 2\int_{\Gamma_{\mathrm{u}}} (\mathbf{u} - \mathbf{u}_{\mathrm{obs}})\cdot\widehat{\mathbf{u}}\,\mathrm{d}s + \int_{\Omega_{\mathrm{c}}} \mathbb{A}\boldsymbol{\mathcal{E}}(\widehat{\mathbf{u}}) : \boldsymbol{\mathcal{E}}(\mathbf{p})\,\mathrm{d}\mathbf{x} = 0. \tag{A.6}$$

It immediately follows from the first relation (A.5) that $\mathbf{u}$ is the unique solution $\mathbf{u}_\Omega$ to the state equation (2.1). From the second relation (A.6), we see that $\mathbf{p}$ is the solution $\mathbf{p}_\Omega$ to the adjoint system (2.7).

Let us now return to the equation (A.3). Taking derivatives with respect to the shape Ω in both sides, the chain rule yields:

$$\forall \mathbf{p} \in V, \quad J'_{\mathrm{LS}}(\Omega)(\boldsymbol{\theta}) = \frac{\partial \mathcal{L}}{\partial \Omega}(\Omega, \mathbf{u}_\Omega, \mathbf{p})(\boldsymbol{\theta}) + \frac{\partial \mathcal{L}}{\partial \mathbf{u}}(\Omega, \mathbf{u}_\Omega, \mathbf{p})(\mathbf{u}'_\Omega(\boldsymbol{\theta})). \tag{A.7}$$

The first partial derivative in the above right-hand side is the derivative of the mapping $\Omega \mapsto \mathcal{L}(\Omega, \mathbf{u}, \mathbf{p})$ (for fixed $\mathbf{u}$, $\mathbf{p} \in V$), which is eventually evaluated at $\mathbf{u} = \mathbf{u}_\Omega$ and $\mathbf{p}$. This quantity is easily computed thanks to

Proposition A.1. The function $\mathbf{u}'_\Omega(\boldsymbol{\theta})$ appearing in the second term is the so-called "Eulerian derivative" of the mapping $\Omega \mapsto \mathbf{u}_\Omega$, i.e.

$$\text{For all } \mathbf{x} \in \Omega_c, \quad \mathbf{u}'_\Omega(\boldsymbol{\theta})(\mathbf{x}) \text{ is the derivative of } \boldsymbol{\theta} \mapsto \mathbf{u}_{\Omega_{\boldsymbol{\theta}}}(\mathbf{x}).$$

Although the latter can be characterized by a boundary value problem, we wish to eliminate this difficult contribution. To achieve this, we now select $\mathbf{p} = \mathbf{p}_\Omega$ in (A.7), so that the second term in the right-hand side of (A.7) vanishes, see (A.6). We are thus left with:

$$J'_{\mathrm{LS}}(\Omega)(\boldsymbol{\theta}) = \frac{\partial \mathcal{L}}{\partial \Omega}(\Omega, \mathbf{u}_\Omega, \mathbf{p}_\Omega)(\boldsymbol{\theta}).$$

A simple calculation based on Proposition A.1 now yields:

$$J'_{\mathrm{LS}}(\Omega)(\boldsymbol{\theta}) = -\int_\Gamma \mathbb{A}\boldsymbol{\mathcal{E}}(\mathbf{u}_\Omega) : \boldsymbol{\mathcal{E}}(\mathbf{p}_\Omega)(\boldsymbol{\theta}\cdot\mathbf{n})\,\mathrm{d}s - \Delta P \int_\Gamma \mathrm{div}(\mathbf{p}_\Omega)(\boldsymbol{\theta}\cdot\mathbf{n})\,\mathrm{d}s,$$

where the sign comes from the fact that the integrals featured in the expression (A.4) of the Lagrangian involve the domain Ω_c, while $\mathbf{n}$ points in the opposite direction as $\mathbf{n}_c$. This is the desired formula.

Text S2. Additional details about the method

This section describes a few specific ingredients of our shape optimization workflow.

Extension-regularization of the descent direction. Let us place ourselves at a given iteration n of the optimization process, omitting the reference to the latter for simplicity. The tempting choice $\boldsymbol{\theta}_\mathbf{d} = -v_\Omega \mathbf{n}$ of a descent direction for the objective function $J_{\mathrm{LS}}(\Omega)$, suggested by the expression (2.6) of the shape derivative $J'_{\mathrm{LS}}(\Omega)(\boldsymbol{\theta})$, is actually awkward in practice: on the one hand, it is only defined on the boundary Γ of the magma domain Ω, while the practice of the Level Set Method requires this field to be defined on the whole computational domain D. On the other hand, this expression often lacks smoothness and thus tends to create unwanted numerical artifacts on the boundaries of the successively updated shapes Ω^n [36].

To circumvent both difficulties, we rely on the so-called Hilbertian method, about which we refer to e.g. [3, 11]. Let us introduce the following bilinear form, acting on scalar fields $u, v : D \to \mathbb{R}$:

$$a(u,v) = \alpha^2 \int_D \nabla u \cdot \nabla \,\mathrm{d}\mathbf{x} + \int_D uv \mathrm{d}\mathbf{x},$$

where α is a regularization length scale, typically of the order of a few times the mesh element size. We then search for v_Ω^{ext} as the solution to the following variational problem

$$\text{Search for } v_\Omega^{\mathrm{ext}} \text{ s.t. for all } w, \quad a(v_\Omega^{\mathrm{ext}}, w) = \int_\Gamma v_\Omega w \,\mathrm{d}s.$$

This task is easily carried out thanks to a standard Finite Element solver. We eventually define the vector field

$$\boldsymbol{\theta_\mathbf{d}}^{\mathrm{ext}} = -v_\Omega^{\mathrm{ext}} \mathbf{n}^{\mathrm{ext}},$$

involving an extension $\mathbf{n}^{\mathrm{ext}} : D \to \mathbb{R}^3$ of the normal vector field to Γ on the whole computational domain D.

The vector field $\boldsymbol{\theta_\mathbf{d}}^{\mathrm{ext}}$ is a regularized descent direction for $J_{\mathrm{LS}}(\Omega)$ defined on the whole domain D. Loosely speaking, it is a smeared version of the "natural" descent direction $\boldsymbol{\theta}_\mathbf{d}$, over a layer around Γ with thickness α.

Line search procedure. At a given optimization iteration, the selection of a suitable step τ scaling the update (2.9) of Ω according to the descent direction $\boldsymbol{\theta_\mathbf{d}}^{\mathrm{ext}}$ is carried out thanks to a classical line search strategy, see e.g. [29]. This procedure ensures that τ is neither "too large" – in which case the Taylor expansion (2.5) would not be valid and the decrease of the objective would not be guaranteed – nor "too small", which would slow down the optimization.

At first, the descent direction $\boldsymbol{\theta_\mathbf{d}}^{\mathrm{ext}}$ resulting from the previous extension-regularization procedure is multiplied by the factor $\frac{h}{||\boldsymbol{\theta_\mathbf{d}}^{ext}||_{L^\infty}}\boldsymbol{\theta_\mathbf{d}}^{ext}$, with h the average element length, and $||\cdot||_{L^\infty}$ the supremum norm. Thus, the resulting vector field imposes a maximum perturbation with magnitude equal to the mesh size h.

An internal loop is then triggered. It starts from an initial value τ for the descent step; because of the aforementioned normalization, the maximum discrepancy between Ω and the updated shape $\Omega_{\tau\boldsymbol{\theta_d}^{\text{ext}}}$ is equal to τ times the mesh size h. We then evaluate the performance $J_{\text{LS}}(\Omega_{\tau\boldsymbol{\theta_d}^{\text{ext}}})$ of this new shape. If

$$J_{\text{LS}}(\Omega_{\tau\boldsymbol{\theta_d}^{\text{ext}}}) \ < \ (1+\texttt{tol})J_{\text{LS}}(\Omega),$$

i.e. $\Omega_{\tau\boldsymbol{\theta_d}^{\text{ext}}}$ is better than Ω, up to a small tolerance `tol` (typically, `tol` $= 0.01$), the step is accepted, and the value of τ is slightly increased in preparation for the line search to be conducted at the next iteration $n+1$. Otherwise, we go back to the beginning of the internal loop after decreasing the value of τ.

Intuitively, when new shapes tend to be better than the previous ones, the step size increases to accelerate the process; on the contrary, it is decreased along "bad" branches of the optimization flow.

Termination criterion. Multiple strategies could be implemented to decide termination of the optimization process: one could for instance rely on the behavior of the minimized objective function $J(\Omega)$, which ceases to decrease and eventually stalls after a certain number of iterations. In this preliminary work, for simplicity, this rationale was applied by a manual monitoring of the values of $J(\Omega)$.

Text S3. Additional comments about the convergence behavior of the method

This section broaches the four general behaviors adopted by our numerical algorithm in the course of the optimization process.

Oftentimes, the first iterations $n = 0, \dots$ feature a "good" descent direction $\boldsymbol{\theta_d}^n$: the shape Ω^n changes significantly, and the corresponding values of the objective function $J_{\text{LS}}(\Omega^n)$ show fast decrease; according to the the line search strategy strategy described in Supplementary Text S2, the step size τ^n grows rapidly. See for instance Fig. 4c.

After this initial phase of fast progress, the algorithm tends to stagnate: the updates of the shape Ω^n entail less and less significant modifications, and the values of the objective function $J_{\text{LS}}(\Omega^n)$ and of the step size τ^n plateau, possibly until termination of the method, where a local minimum is attained. See iterations 100 to $1,000$ in Fig. 4c.

The shape may run into a "bad" local minimum of $J_{\text{LS}}(\Omega)$ during optimization. The algorithm may then either have difficulties escaping this trap, or it may downright stay stuck. This behavior is exemplified by iterations 250 and 500 on Fig. 3a. There, the values of the objective function $J_{\text{LS}}(\Omega^n)$ show successive bumps: they slightly increase, as the step size τ^n decreases, until a shape with a good descent direction is eventually obtained; then, a more efficient optimization stage begins, during which the objective values drop, until the next local minimum is attained.

Last but not least, let us report on a somewhat undesirable behavior. In some peculiar, "hard" problems, the algorithm may not find a convenient decrease direction for the objective function, and then cause the shape to shrink until vanishing – the empty shape being a "bad" local minimum of the optimization process. To circumvent this behavior, we may compare the initial value $J_{\text{LS}}(\Omega^0)$ of the objective with that $J_{\text{LS}}(\emptyset) = \int_{\Gamma_{\text{u}}} |\mathbf{u}_{\text{obs}}|^2 \mathrm{d}s$ associated to the empty shape $\emptyset$ (inducing $\mathbf{0}$ displacement): if $J_{\text{LS}}(\Omega^0) > J_{\text{LS}}(\emptyset)$, the undesirable vanishing phenomenon may occur, as a valid way to minimize the objective. This indicates that a more relevant initial guess Ω^0, closer to the sought shape of the magma domain, should be chosen. Unfortunately, this difficulty may arise not only at the initial stage, but also in the course of the optimization process, when no "satisfactory" descent direction is found, notably when a too coarse mesh prevents refinement and improvement of the shape. An example of such situation is illustrated in figure 6, where after successfully dividing the shape in two disconnected bodies, the descent stays stuck and the shape shrinks.

In order to help handling the algorithm, and notably tuning the aforementioned behaviors, a tutorial is available alongside the source code at [34], where the main parameters of the method are described and their influence on the optimization process is explained.

Text S4. Definition of the modified objective function $J_{\text{LS}}^{\text{los}}(\Omega)$ used in the treatment of InSAR data

As mentioned in the main text, the comparison of the predicted displacement $\mathbf{u}_\Omega$ of the crust via the numerical resolution of the elasticity system (2.1) to the input InSAR data demands a slight modification of the least-square error $J_{\mathrm{LS}}(\Omega)$ used as the objective function of the problem (2.2). Indeed, the InSAR data is a collection of line-of-sight (LOS) displacements: we only observe the projection of the displacement on the LOS vector of the satellite

$$\mathbf{l} = -\cos(\alpha)\sin(\theta)\mathbf{e_e} + \sin(\alpha)\sin(\theta)\mathbf{e_n} + \cos(\theta)\mathbf{e_u},$$

where α is the heading angle between the projected satellite flight path and the north direction, θ is the inclination angle between the vertical direction and the satellite flight path, and $\mathbf{e_e}$, $\mathbf{e_n}$, $\mathbf{e_u}$ are the unit vectors oriented respectively in the East, North and vertical directions [20]. Hence, we define the LOS least-square error by:

$$J_{\mathrm{LS}}^{\mathrm{los}}(\Omega) = \int_{\Gamma_{\mathrm{u}}} \sum_{i\in\mathtt{tck}} w_i k_i (\mathbf{u}_\Omega \cdot \mathbf{l}_i - d_i^{\mathrm{obs}})^2 \,\mathrm{d}s \tag{A.8}$$

where

$$\mathtt{tck} = \Big\{\mathtt{S1\text{-}T16,\ S1\text{-}T155,\ CSK\text{-}A33,\ CSK\text{-}D44,\ TSX\text{-}T26,\ TSX\text{-}T19}\Big\}$$

is the list of the $N = 6$ used tracks. For each $i = 1, \dots, N$, $w_i = 1/N$ is the weight of the i^{th} track, k_i is a function defined on Γ_u, taking the value 1 in regions where the data coverage is deemed sufficient and 0 where the track has no data (typically on water and glaciers), $\mathbf{l}_i$ is the LOS unit vector of the track, and d_i^{obs} is the observed displacement in the direction $\mathbf{l}_i$.

The shape derivative of this new objective function has a similar structure to that of the function $J_{\mathrm{LS}}(\Omega)$ in (2.6). Arguing as in Supplementary Text S1, we indeed show that:

$$J_{\mathrm{LS}}^{\mathrm{los}\prime}(\Omega)(\boldsymbol{\theta}) = -\int_\Gamma \Big(\mathbb{A}\boldsymbol{\mathcal{E}}(\mathbf{u}_\Omega) : \boldsymbol{\mathcal{E}}(\mathbf{p}_\Omega) + \Delta P \,\mathrm{div}(\mathbf{p}_\Omega)\Big)\,(\boldsymbol{\theta}\cdot\mathbf{n})\,\mathrm{d}s,$$

where the adjoint state $\mathbf{p}_\Omega$ is now the solution to the following system:

$$\begin{cases} -\mathrm{div}(\mathbb{A}\boldsymbol{\mathcal{E}}(\mathbf{p}_\Omega)) = \mathbf{0} & \text{in } \Omega_{\mathrm{c}}, \\ \mathbf{p}_\Omega = \mathbf{0} & \text{on } \Gamma_{\mathrm{b}}, \\ \mathbb{A}\boldsymbol{\mathcal{E}}(\mathbf{p}_\Omega)\mathbf{n}_{\mathrm{c}} = \mathbf{0} & \text{on } \Gamma, \\ \mathbb{A}\boldsymbol{\mathcal{E}}(\mathbf{p}_\Omega)\mathbf{n} = \mathbf{0} & \text{on } \partial D \setminus (\overline{\Gamma_{\mathrm{u}}} \cup \overline{\Gamma_{\mathrm{b}}}), \\ \mathbb{A}\boldsymbol{\mathcal{E}}(\mathbf{p}_\Omega)\mathbf{n} = -2\displaystyle\sum_{i\in\mathtt{tck}} \mathbf{l}_i w_i k_i (\mathbf{u}_\Omega\cdot\mathbf{l}_i - d_i^{\mathrm{obs}}) & \text{on } \Gamma_{\mathrm{u}}. \end{cases}$$

Figures S1 to S5. Additional views for the test cases presented in the main text and additional test cases.

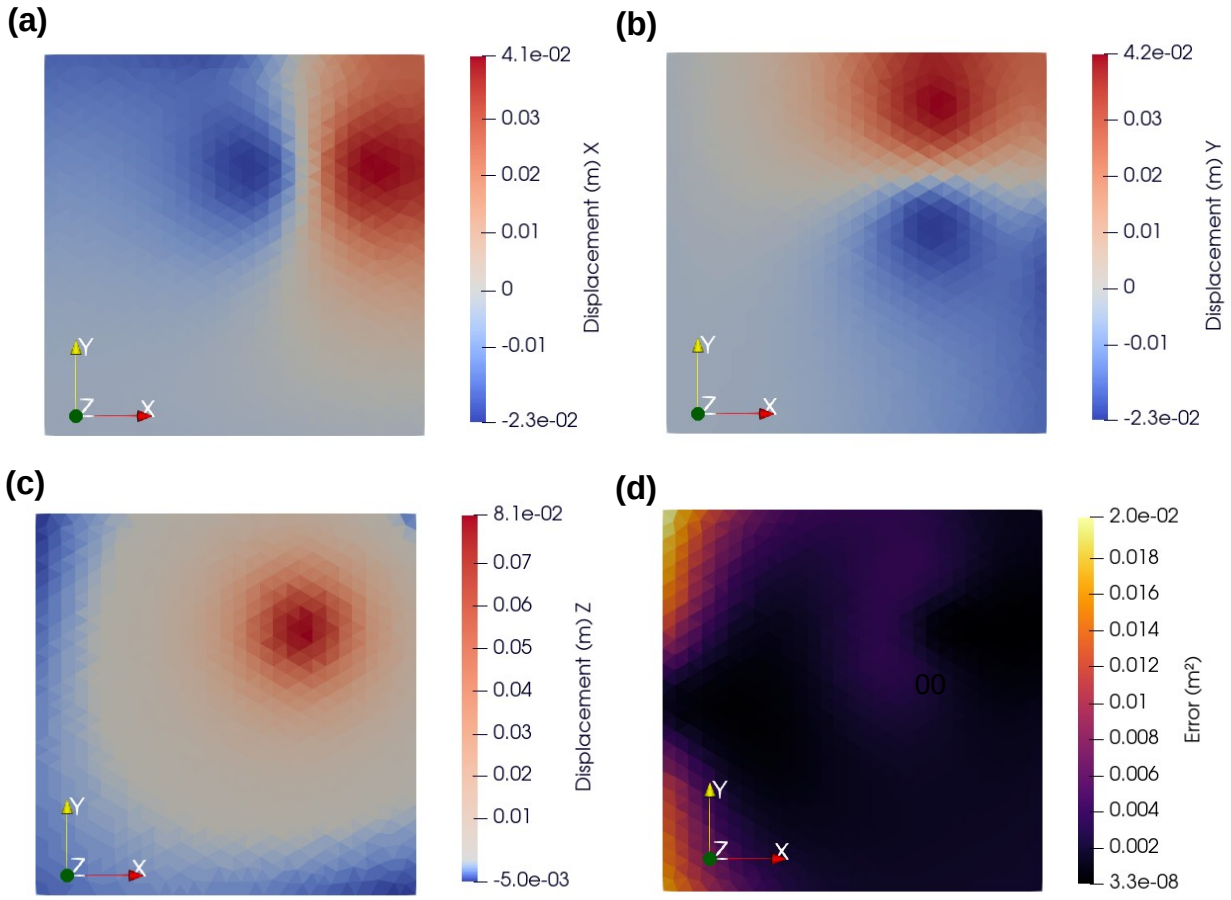

FIGURE 5. *Maps of the upper surface displacement fields for the test case of Section 3.1 in the main text. The width of the geographical region D equals 10 km. Panels (a,b,c) depict the X, Y, Z components of the displacement field, respectively. (d) shows the values of the error* $|\boldsymbol{u}_{\Omega_0} - \boldsymbol{u}_{\Omega*}|^2$ *at the initial stage* ($n = 0$)*: this error takes large values in two regions: over the initial shape* Ω_0*, shaped as an ellipsoid on the left (see Fig. 3) (here, edge effects are expected to be significant), and over the left side of the objective shape* Ω^**, because this is were the discrepancy is maximum: in there,* Ω_0 *induces displacements oriented towards* $+X$ *while* Ω^* *induces displacement oriented towards -X.*

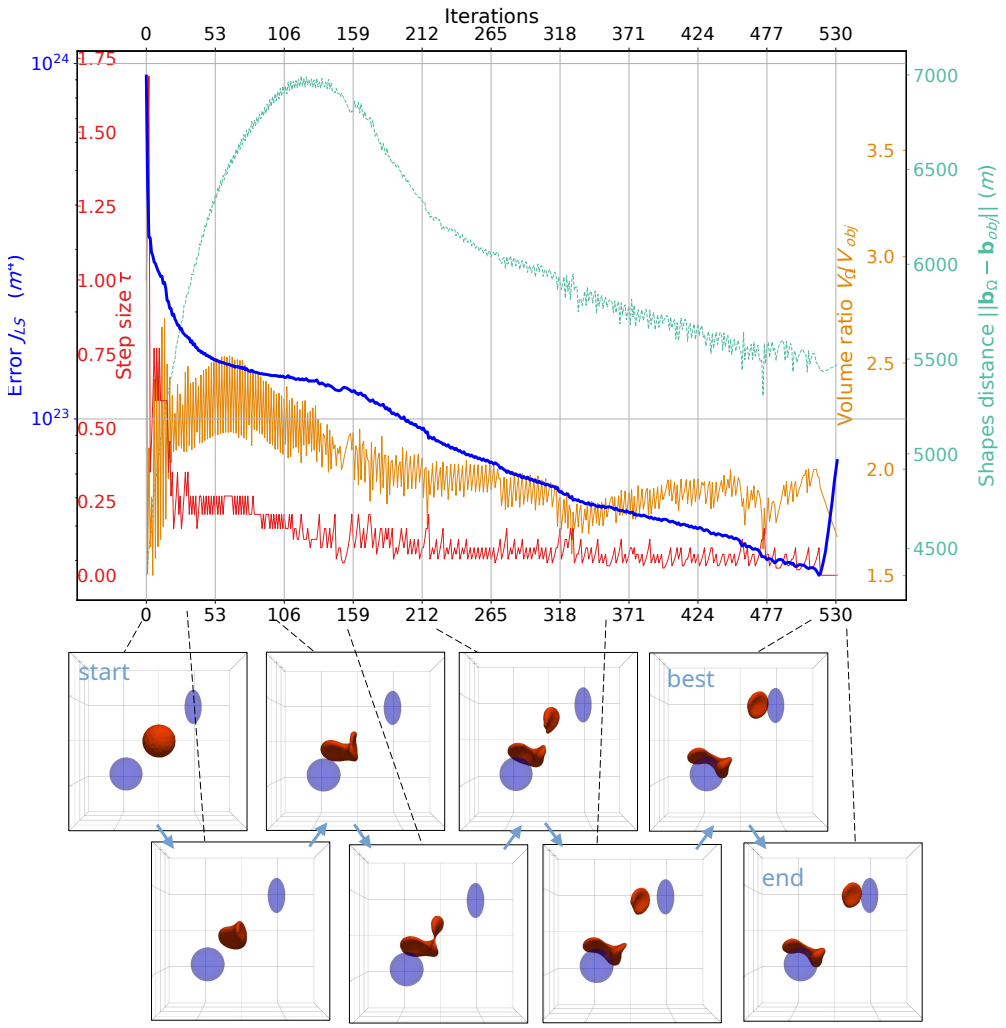

FIGURE 6. *Additional synthetic reconstruction test case; for an explanation of the panels, see Fig. 3 in the main text. Here the target shape Ω^* is made of two disconnected bodies, an ellipsoid (with radii r_x=r_z=1 km, r_y=2 km) located North-East at 3 km depth, and a thick disk (radices r_x=r_y=2 km, r_z=1.5 km) centered South-East at 5 km depth. The initial shape Ω^0 is a sphere with 2 km radius centered at 4 km depth. The best shape is obtained at iteration 517; thereafter, no good direction is found and the volume shrinks. The procedure is stopped after 15 iterations without improvement of the values of the objective function, indicating that the descent process is trapped in a local minima.*

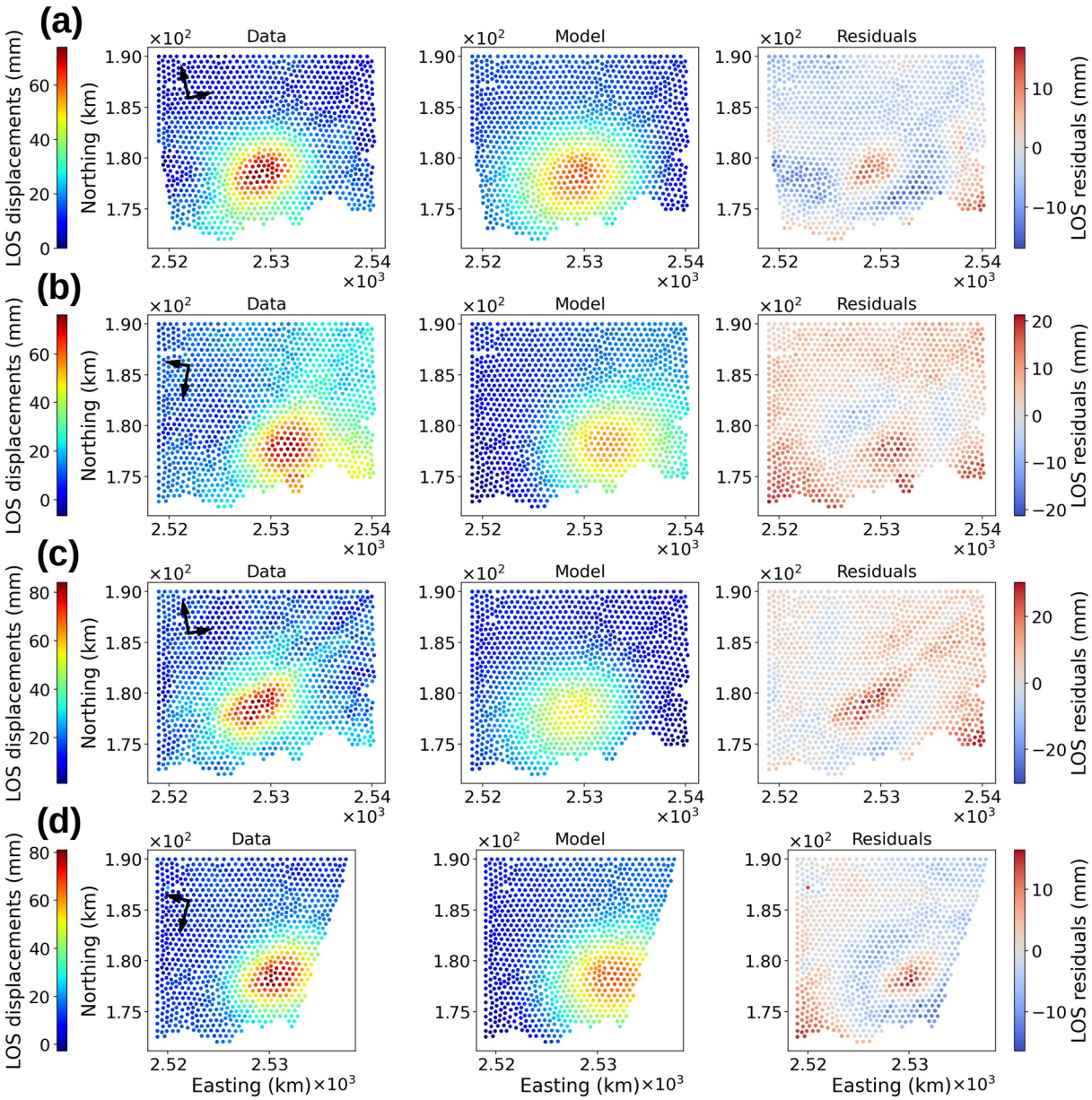

FIGURE 7. *Additional tracks for the InSAR data inversion experiment presented in main text. The columns from left to right correspond to data, models and residuals, respectively. The tracks COSMO-Skymed ascending A33 and descending D44 are depicted in rows a) and b), and TerraSAR-X ascending T26 and descending T19 are depicted in rows c) and d).*

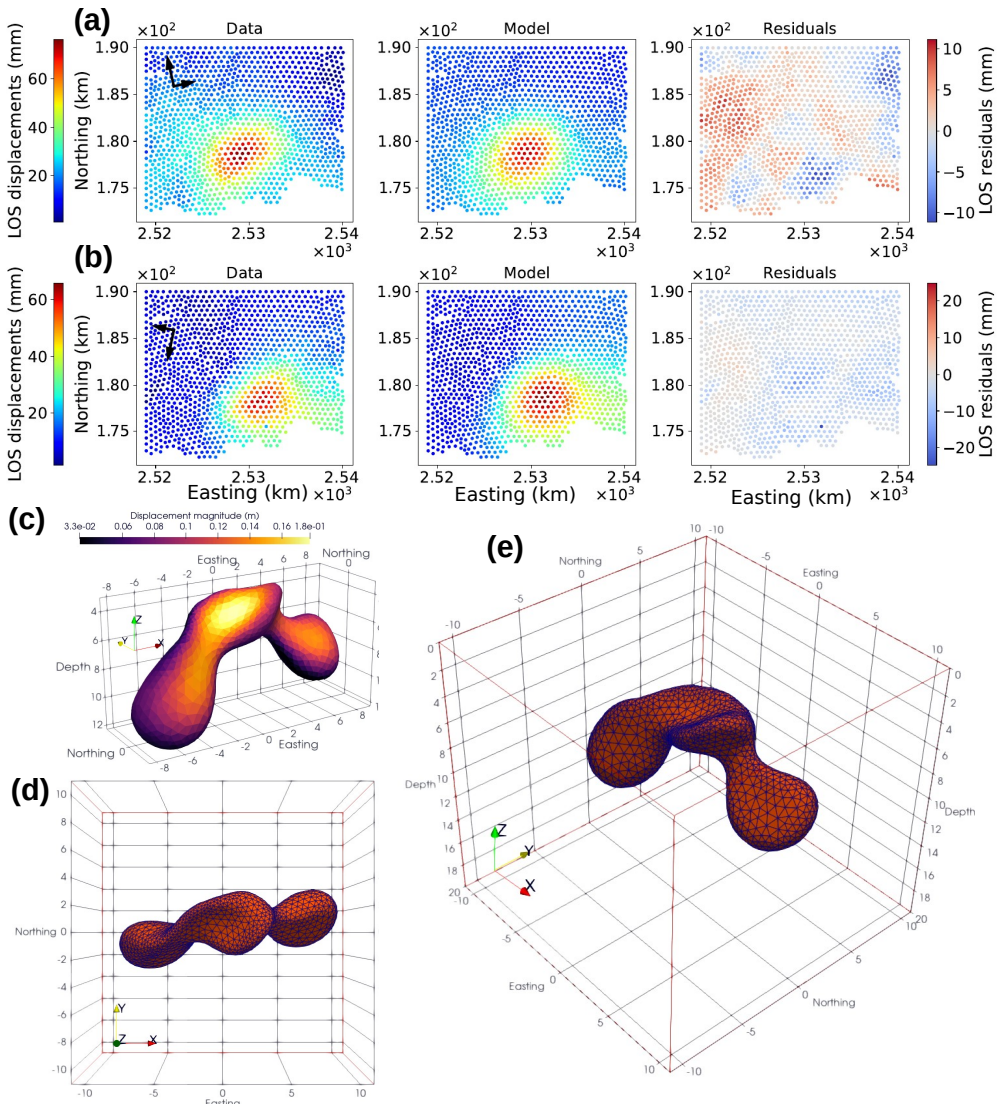

FIGURE 8. *Optimal shape of a magma domain based on the data from the Svarstengi 2022 inflation event, assuming a pressure change of* $\Delta P = 1$ MPa. *The represented panels are the same as in Fig. 4, except for the convergence history which shows similar trends. Here, the total volume of the optimal shape equals* 179 km^3 *(*$\approx$ *5 times larger than in the example of Fig. 4), producing a volume change of* $\Delta V = 20 \times 10^6$ *(about the same as in Fig. 4). The shape is centered at* $(-0.1,\ 0.2,\ -7.7)$ km*; it is* 17 km *elongated in the East-West direction, ranging from* 3 km *to* 12 km *depth. It features 3 lobes from* 1 *to* 3 km *thick. The proximity of the edges of the computational domain with the magma domain in this case certainly influences the results.*

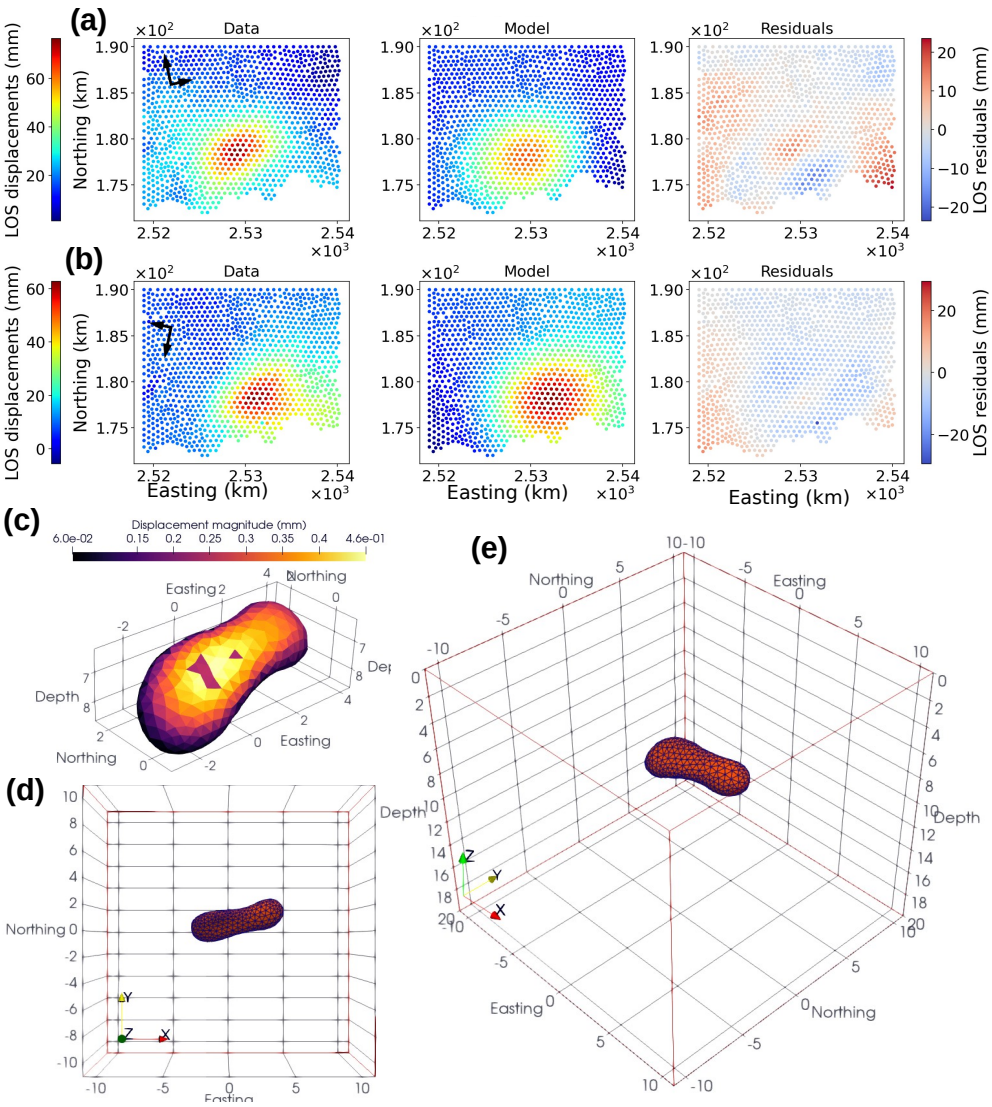

FIGURE 9. *Optimal shape of a magma domain based on the data from the Svarstengi 2022 inflation event, assuming a pressure change of* $\Delta P = 6$ MPa. *The total volume of the optimized shape equals* 16 km^3 *(about twice as small than that in Fig. 4), and the latter causes a volume change of* $\Delta V = 11 \times 10^6$ *(about the same as in Fig. 4). The shape is centered at* $(0.7,\ 0.8,\ -7.3)$ km. *It is* 7.5 *km elongated in the East-West direction, ranges from* 3 km *to* 12 km *depth, is about* $0.9 - 1.5$ km *thick, dipping south of about* $36°$.

Movie S1. Evolution of the shape during the optimization for the synthetic test case (Section 3.1.)

The left panel depicts a 3D view of the current shape Ω^n in red while the target shape Ω^* is the transparent blue sphere. The computational domain D is outlined with gray lines. The lower right panel is a top view of the situation. The upper right panel contains the convergence history of the computation: the values of the objective $J_{\mathrm{LS}}(\Omega^n)$ are represented by the red curve, the curve for the step size is in blue and the current iteration is indicated with the dashed orange line. During the optimization, the step size τ^n resulting from the line search procedure is oscillating because of the occasional difficulty to find a suitably small value, which accordingly causes small oscillations of the volume of the shape .

Movie S2. Evolution of the shape during the optimization for the real data test case (Section 3.2).

The panels are the same as for Movie S1.

References

[1] G. Allaire, *Conception Optimale de Structures*, vol. 58 of Mathématiques & Applications, Springer Berlin Heidelberg, 2006.

[2] G. Allaire, C. Dapogny, and P. Frey, *Shape optimization with a level set based mesh evolution method*, Computer Methods in Applied Mechanics and Engineering, 282 (2014), pp. 22–53.

[3] G. Allaire, C. Dapogny, and F. Jouve, *Shape and topology optimization*, in Handbook of numerical analysis, vol. 22, Elsevier, 2021, pp. 1–132.

[4] G. Allaire, F. Jouve, and A.-M. Toader, *Structural optimization using sensitivity analysis and a level-set method*, Journal of computational physics, 194 (2004), pp. 363–393.

[5] H. Azegami, *Shape Optimization Problems*, Springer, 2020.

[6] M. Bagnardi and A. Hooper, *Inversion of Surface Deformation Data for Rapid Estimates of Source Parameters and Uncertainties: A Bayesian Approach*, Geochemistry, Geophysics, Geosystems, 19 (2018), pp. 2194–2211.

[7] G. Balarac, F. Basile, P. Bénard, F. Bordeu, J.-B. Chapelier, L. Cirrottola, G. Caumon, C. Dapogny, P. Frey, A. Froehly, et al., *Tetrahedral remeshing in the context of large-scale numerical simulation and high performance computing*, MathematicS In Action, 11 (2022), pp. 129–164.

[8] M. P. Bendsoe and O. Sigmund, *Topology Optimization by Distribution of Isotropic Material*, in Topology Optimization: Theory, Methods, and Applications, M. P. Bendsoe and O. Sigmund, eds., Springer, Berlin, Heidelberg, 2004, pp. 1–69.

[9] M. P. Bendsoe and O. Sigmund, *Topology optimization: theory, methods, and applications*, Springer Science & Business Media, 2013.

[10] C. Bui, C. Dapogny, and P. Frey, *An accurate anisotropic adaptation method for solving the level set advection equation*, International Journal for Numerical Methods in Fluids, 70 (2012), pp. 899–922.

[11] M. Burger, *A framework for the construction of level set methods for shape optimization and reconstruction*, Interfaces and Free boundaries, 5 (2003), pp. 301–329.

[12] J. Cea, *Conception Optimale Ou Identification de Formes, Calcul Rapide de La Dérivée Directionnelle de La Fonction Coût*, ESAIM: Modélisation mathématique et analyse numérique, 20 (1986), pp. 371–402.

[13] P. Cervelli, M. H. Murray, P. Segall, Y. Aoki, and T. Kato, *Estimating Source Parameters from Deformation Data, with an Application to the March 1997 Earthquake Swarm off the Izu Peninsula, Japan*, Journal of Geophysical Research: Solid Earth, 106 (2001), pp. 11217–11237.

[14] M. Charco and P. Galán del Sastre, *Efficient Inversion of Three-Dimensional Finite Element Models of Volcano Deformation*, Geophysical Journal International, 196 (2014), pp. 1441–1454.

[15] C. Dapogny, C. Dobrzynski, and P. Frey, *Three-dimensional adaptive domain remeshing, implicit domain meshing, and applications to free and moving boundary problems*, Journal of computational physics, 262 (2014), pp. 358–378.

[16] C. Dapogny and F. Feppon, *Shape Optimization Using a Level Set Based Mesh Evolution Method: An Overview and Tutorial*, Comptes Rendus. Mathématique, 361 (2023), pp. 1267–1332.

[17] C. Dapogny and P. Frey, *Computation of the signed distance function to a discrete contour on adapted triangulation*, Calcolo, 49 (2012), pp. 193–219.

[18] F. Feppon, G. Allaire, and C. Dapogny, *Null space gradient flows for constrained optimization with applications to shape optimization*, ESAIM: Control, Optimisation and Calculus of Variations, 26 (2020), p. 90.

[19] F. Feppon, G. Allaire, C. Dapogny, and P. Jolivet, *Topology Optimization of Thermal Fluid–Structure Systems Using Body-Fitted Meshes and Parallel Computing*, Journal of Computational Physics, 417 (2020), p. 109574.

[20] T. Fuhrmann and M. C. Garthwaite, *Resolving three-dimensional surface motion with insar: Constraints from multi-geometry data fusion*, Remote Sensing, 11 (2019).

[21] C. Geuzaine, J.-F. Remacle, and P. Dular, *Gmsh: A Three-Dimensional Finite Element Mesh Generator*, International Journal for Numerical Methods in Engineering, 79 (2009), pp. 1309–1331.

[22] F. Hecht, *New Development in FreeFem++*, Journal of Numerical Mathematics, 20 (2012), pp. 251–265.
[23] A. Henrot and M. Pierre, *Shape variation and optimization*, EMS Press, 2018.
[24] J. Hickey and J. Gottsmann, *Benchmarking and Developing Numerical Finite Element Models of Volcanic Deformation*, Journal of Volcanology and Geothermal Research, 280 (2014), pp. 126–130.
[25] F. Lucchini, R. Torchio, V. Cirimele, P. Alotto, and P. Bettini, *Topology optimization for electromagnetics: A survey*, IEEE Access, 10 (2022), pp. 98593–98611.
[26] D. F. McTigue, *Elastic Stress and Deformation near a Finite Spherical Magma Body: Resolution of the Point Source Paradox*, Journal of Geophysical Research: Solid Earth, 92 (1987), pp. 12931–12940.
[27] K. Mogi, *Relations between the Eruptions of Various Volcanoes and the Deformations of the Ground Surfaces around Them*, Earthq Res Inst, 36 (1958), pp. 99–134.
[28] F. Murat and J. Simon, *Sur le contrôle par un domaine géométrique*, Preprint of the Laboratoire d'Analyse Numérique, (1976).
[29] J. Nocedal and S. J. Wright, *Numerical optimization 2nd*, Springer, 2006.
[30] Y. Okada, *Surface deformation due to shear and tensile faults in a half-space*, Bulletin of the Seismological Society of America, 75 (1985), pp. 1135–1154.
[31] S. Osher and R. Fedkiw, *Level set methods and dynamic implicit surfaces*, vol. 153, Springer Science & Business Media, 2006.
[32] S. Osher and J. A. Sethian, *Fronts propagating with curvature-dependent speed: Algorithms based on hamilton-jacobi formulations*, Journal of computational physics, 79 (1988), pp. 12–49.
[33] M. Parks, V. Drouin, H. Geirsson, A. Hooper, S. Hreinsdóttir, B. Ófeigsson, H. M. Friðriksdóttir, K. S. Vogfjörd, C. Lanzi, and V. Tolpekin, *Data and Geodetic Modelling Results for Science Article "Fracturing and Tectonic Stress Drives Ultra-Rapid Magma Flow into Dikes"*, Jan. 2024.
[34] T. Perrot, *magmaopt*. https://github.com/Th2ooo/magmaOpt, 2025.
[35] O. Pironneau, *Optimal shape design for elliptic systems*, Springer, 1982.
[36] ———, *Applied shape optimization for fluids*, Oxford university press, 2010.
[37] R.-E. Plessix, *A review of the adjoint-state method for computing the gradient of a functional with geophysical applications*, Geophysical Journal International, 167 (2006), pp. 495–503.
[38] J. Sethian, *Level set methods and fast marching methods*, Cambridge University, (1999).
[39] O. Sigmund and K. Maute, *Topology Optimization Approaches: A Comparative Review*, Structural and Multidisciplinary Optimization, 48 (2013), pp. 1031–1055.
[40] F. Sigmundsson, M. Parks, H. Geirsson, A. Hooper, V. Drouin, K. S. Vogfjörd, B. G. Ófeigsson, S. H. M. Greiner, Y. Yang, C. Lanzi, G. P. De Pascale, K. Jónsdóttir, S. Hreinsdóttir, V. Tolpekin, H. M. Friðriksdóttir, P. Einarsson, and S. Barsotti, *Fracturing and Tectonic Stress Drives Ultrarapid Magma Flow into Dikes*, Science, (2024), p. eadn2838.
[41] F. Sigmundsson, M. Parks, A. Hooper, H. Geirsson, K. S. Vogfjörd, V. Drouin, B. G. Ófeigsson, S. Hreinsdóttir, S. Hjaltadóttir, K. Jónsdóttir, P. Einarsson, S. Barsotti, J. Horálek, and T. Ágústsdóttir, *Deformation and seismicity decline before the 2021 Fagradalsfjall eruption*, Nature, 609 (2022), pp. 523–528. Publisher: Nature Publishing Group.
[42] J. Sokolowski and J.-P. Zolésio, *Introduction to shape optimization*, in Introduction to Shape Optimization: Shape Sensitivity Analysis, Springer, 1992, pp. 5–12.
[43] E. Trasatti, *Volcanic and Seismic Source Modeling: An Open Tool for Geodetic Data Modeling*, Frontiers in Earth Science, 10 (2022).
[44] G. T. Valssson, *ISN2016 - Tækniskýrsla*, tech. rep., Landmælingar, Íslands, Mar. 2019.
[45] M. L. Velez, P. Euillades, A. Caselli, M. Blanco, and J. M. Díaz, *Deformation of Copahue Volcano: Inversion of InSAR Data Using a Genetic Algorithm*, Journal of Volcanology and Geothermal Research, 202 (2011), pp. 117–126.
[46] X.-M. Yang, P. M. Davis, and J. H. Dieterich, *Deformation from Inflation of a Dipping Finite Prolate Spheroid in an Elastic Half-Space as a Model for Volcanic Stressing*, Journal of Geophysical Research: Solid Earth, 93 (1988), pp. 4249–4257.